Hyperspectral Denoising via Global Variation and Local Structure Low-Rank Model

Lan Li, Meiping Song, *Member, IEEE*, Qiang Zhang, *Member, IEEE*, and Yushuai Dong

***Abstract*— Hyperspectral images (HSIs) are often disturbed by various kinds of noises. This article proposes a global variation and local structure low-rank model (GLLR) for HSI denoising by integrating spatial segmentation smoothing and spectral low-rank (LR) properties. Compared with existing denoising methods, the proposed method considers not only the global LR property but also the local structure LR property of HSIs. Specifically, the GLLR describes the global correlation and segmental smoothing structure of the HSI by the correlated total variation (CTV). In addition, we construct a new structural LR prior, called the local minimum difference (LMD) LR. With LMD LR property of HSI, GLLR can remove noise while retaining useful structural information in the HSI. Then, an augmented lagrange multiplier (ALM)-based optimization algorithm is devised to solve the objective functions for the presented model. Finally, comparison experiments with existing methods are conducted on synthetic and real datasets to demonstrate the effectiveness and superiority of the proposed method.**

***Index Terms*— Alternating iterative optimization, denoise, hyperspectral image (HSI), local structure, low-rank (LR).**

I. INTRODUCTION

THERE are hundreds of spectral bands and rich texture information in the hyperspectral image (HSI) with wide applications, such as classification [1], [2], [3], [4], [5], [6] and the anomaly or target detection [7], [8], [9], to name a few. Due to sensor tremor, atmospheric interference, and signal response, HSI inevitably suffers from various types of noise in the collection process, including Gaussian noise, salt and pepper noise, stripe noise, and mixed noise [10]. These noises degrade the quality of HSI and bring challenges to the subsequent analysis and application. For tasks like land cover change detection, accurate image information is crucial as it reveals changes in land use and cover [11], [12], [13]. The denoising operation of remote sensing images can improve image quality and enhance the visibility of land transformation features. Thus, it improves the effectiveness and reliability of land cover change detection. It is seen that the denoising operation is necessary and beneficial for remote sensing images.

Numerous denoising methods [14], [15], [16], [17], [18] have been presented to handle the noise in HSI. Due to the unique 1-D spectral domain of HSI, the denoising technique for HSI has a different requirement from natural image containing only 2-D spatial domain. It is crucial to simultaneously preserve spectral features and eliminate mixed noise from various bands. Thus, it leads to distorted or unsatisfactory denoising results by using 1-D or 2-D denoising methods. It is noted that the denoising performance can be enhanced by utilizing the distinctive spatial and spectral correlation of HSI [19]. Up to now, there are some denoising methods for HSI with its redundant and complementary information to eliminate noise [20], [21], [22]. Such as nonlocal spatial self-similarity [23], [24], which considers the similarity between different pixels and nonlocal patches. Total variation (TV) [25], [26], effectively preserves the edge features of HSI. Sparse representation-based methods [27] utilize spectral redundancy, but such methods often fail to fully exploit the spatial correlations of 3-D data [10]. And low-rank (LR) model [28], [29], effectively capture the spectral redundancy of HSI, preserving both the spatial and spectral information within the data. For HSI, the spectral LR is regarded as the inherent prior knowledge and is widely used in image restoration [30]. The LR model proposes in [28] and [29] can capture the spectral redundancy of HSI to preserve the spatial and spectral information of data. With GoDec theory, Zhang et al. [31] proposes an LR matrix recovery (LRMR)-based denoising method to remove mixed noise in HSI. Peng et al. [32] propose a reweighted LR matrix restoration method to improve the quality of image or video. Considering the local structure and high spectral correlation of the original HSI, Lu et al. [33] develop a graph-regularized LR model regarded as an extension of the original LR model. Principal component analysis proposes in [34], one of the most famous LR-based method aims to convert the HSI into a set of linearly uncorrelated variables via an orthogonal transformation. This classical method ignores the local smoothness (LS) of neighborhood pixels in the spatial dimension. Moreover, it is sensitive to outliers [35].

Since piecewise smooth property of HSI in the spatial dimension, the TV regularization technique is widely used for HSI restoration [36] and anomaly detection [37], [38], [39]. In [25], the spectral–spatial adaptive TV (SSTV) is developed for the HSI denoising by differences between the noise intensity and spatial information. Chen et al. [40] propose an HSI denoising model based on the TV regularized bilinear factorization. The methods presented in [25] and [40] achieved remarkable results in the field of HSI denoising. However, they exhibit a negative impact on the pixel values that remain unaffected by the impulse [35].

Manuscript received 25 April 2023; revised 10 August 2023 and 5 September 2023; accepted 12 September 2023. Date of publication 25 September 2023; date of current version 4 October 2023. This work was supported in part by the National Natural Science Foundation of China under Grant 61971082. *(Corresponding authors: Meiping Song; Qiang Zhang.)*

The authors are with the Information and Technology College, Dalian Maritime University, Dalian 116026, China (e-mail: lanli@dlmu.edu.cn; smping@163.com; qzhang95@dlmu.edu.cn; 15047694784@163.com).

Digital Object Identifier 10.1109/TGRS.2023.3318521

To improve the performance of the HSI denoising, He et al. [35], [42], Wang et al. [41], and Peng et al. [43] present the denoising methods combining the LR prior with the TV regularization. Specifically, He et al. [35] investigate the LRTV method, which employs the LR model to depict spectral correlation and the TV model to capture the spatial local smooth structure. Wang et al. [41] utilize the weighted nuclear norm and SSTV model to recover the clean HSI. He et al. [42] propose the rank-constrained LRMR to separate the LR components from sparse noise, and capture the global spatial-spectral LS property with SSTV. Recently, Peng et al. [43] establish a correlated TV (CTV) regularization term to develop a CTV-robust principal component analysis (RPCA) model, which can separate the joint LR and LS parts as well as the sparse part.

In recent years, the deep learning (DL)-based technique has been gradually applied to HSI [44], [45], [46], such as HSI recovery [47], [48], [49], [50], [51], [52], [53] and super-resolution [54], [55], [56]. Based on the spatial–spectral gradient learning strategy, a spatial–spectral gradient network is presented for mixed noise removal in [51]. Considering the local and global information of HSI, a deep spatial-spectral global reasoning network is established for the HSI denoising in [49]. Maffei et al. [45] proposes a single denoising convolutional neural network (CNN) model for HSI denoising. A model-guided interpretable network for the HSI denoising is presented by utilizing spatial and spectral information [50]. Utilizing the spatial-spectral deep CNN, Yuan et al. [52] devise a DL-based HSI denoising method to learn the mapping between noise and original HSI.

Existing global LR and TV models focus mostly on the overall properties of HSI and ignore the local structural features disrupted by noise. The local features are critical to preserving spatial details and handling mixed noise since they can reveal texture characteristics in different regions. In order to achieve both global and local structure recovery, this article develops an HSI restoration method based on global variation and local structural LR properties. The proposed method incorporates the prior knowledge of noise HSI and introduces the local structural information into a unified HSI denoising framework, which can capture local details to improve the restoration performance for noise-disrupted HSI. To fully demonstrate the effectiveness and superiority of the proposed method in handling mixed noise, this article conducts and analyzes comparative experiments on multiple sets of simulated and real data containing mixed noise scenarios. The main contributions of this article are summarized as follows.

1) This article establishes a unified HSI denoising framework based on a comprehensive modeling strategy. The established framework takes into account the global variation and local structural LR properties, which enables better restoration of clean signals under mixed noise scenarios.
2) A local structural feature of an HSI is defined and constructed as a Casorati matrix. With the aid of its LR property, the Casorati matrix is capable of representing the local structural features of HSI.
3) Extensive comparative and ablation experiments under multiple degradation scenarios are implemented to validate the effectiveness and robustness of the proposed method for denoising tasks of HSI subject to different types of mixed noise.

The rest parts are arranged as follows. Section II introduces the problem formulation and related method. Section III derives the proposed global variation and local structure LR model (GLLR). Section IV conducts and analyzes comparative experiments on synthetic and real datasets. Section V concludes this article.

II. PROBLEM FORMULATION AND RELATED METHOD

A. Problem Formulation

Since the acquired HSI is disturbed by mixed noise, its degradation formula can be described as

$$\mathbf{Y} = \mathbf{X} + \mathbf{N} + \mathbf{S} \tag{1}$$

where $\mathbf{Y}$ is the noisy HSI. $\mathbf{X}$ represents the desired clean HSI. $\mathbf{N}$ and $\mathbf{S}$ denote the random additive noise and the sparse error, respectively. The size of $\mathbf{Y}$, $\mathbf{X}$, $\mathbf{N}$, and $\mathbf{S}$ is $hw \times b$ with h, w, and b being the spatial and spectral dimensions of the HSI, respectively. Obviously, it is an ill-posed problem to solve $\mathbf{X}$ using $\mathbf{Y}$ from (1).

B. Low Rank Model

Consider integrating the LR and LS priors of HSI into one regularization term, CTV-RPCA [43] advocates using a nuclear norm to describe the correlation between gradient images, and defined CTV regularization. Then the CTV-RPCA to separate the joint LR and LS part $\mathbf{X}$ from the sparse part $\mathbf{S}$. Similar to the traditional RPCA problem, they describe the given observation data $\mathbf{Y}$ and the unknown LR matrix ($\mathbf{X}$ or $\nabla\mathbf{X}$) and sparse error matrix $\mathbf{S}$, with the goal of recovering $\mathbf{X}$. The optimization problem is stated as follows:

$$\begin{aligned} \min_{\mathbf{X},\mathbf{S}} \ & \sum_{i=1}^{3} \|\mathbf{H}_i\|_* + 3\lambda_1 \|\mathbf{S}\|_1 \\ \text{s.t. } & \mathbf{Y} = \mathbf{X} + \mathbf{S} \\ & \nabla_i(\mathbf{X}) = \mathbf{H}_i. \end{aligned} \tag{2}$$

Zhou et al. [57] recovered LR matrices from high-dimensional data disrupted by small entrywise noise and gross sparse errors. That is, assuming $\mathbf{Y} = \mathbf{X} + \mathbf{N} + \mathbf{S}$, where $\mathbf{Y}$, $\mathbf{X}$, $\mathbf{S}$ and $\mathbf{N}$ are consistent with the previous description. Similarly, the model for solving this problem can be written as

$$\begin{aligned} \min_{\mathbf{X},\mathbf{S}} \ & \|\nabla\mathbf{X}\|_* + \lambda\|\mathbf{S}\|_1 \\ \text{s.t. } & \|\mathbf{Y} - \mathbf{X} - \mathbf{S}\|_F \le \delta \end{aligned} \tag{3}$$

where δ is a constant associated with the random noise $\mathbf{N}$.

III. PROPOSED HSI RESTORATION METHOD

The minimum and $|\cdot|$ operations are regard as mapping matrices [58], and define as $\mathbf{M}$ and as $\mathbf{A}$, respectively.

A. $\mathbf{M}$ and $\mathbf{A}$ Operator

Note that there are three dimensions involved in the difference operator, i.e., $\nabla = (\nabla_1, \nabla_2, \nabla_3)^T$, where, ∇_1, ∇_2

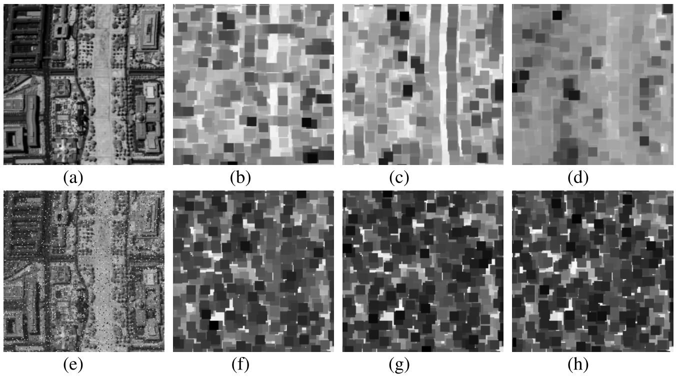

Fig. 1. Local structural features of the image with noise interfere. (a) Original. (b) Vertical. (c) Horizontal. (d) Spectral. (e) Noisy. (f) Vertical. (g) Horizontal. (h) Spectral.

and ∇_3 represent the difference in the horizontal, vertical, and spectral directions, respectively. Therefore, the absolute operator is also involved 3-D, i.e., $A = (A_1, A_2, A_3)$, which is given by

$$A_1(x,y) = \begin{cases} 1, & \text{if } \nabla_1 X(x,y) \geq 0 \\ -1, & \text{if } \nabla_1 X(x,y) < 0. \end{cases} \tag{4}$$

Similar for A_2 and A_3. Then,

$$|\nabla X| = A \odot \nabla X \tag{5}$$

where $\odot$ denotes a hadamard product, operators A and ∇ should be sparse in vector form of X. In this case, we rewrite A in diagonal form. Then, $|\nabla \mathbf{X}| = \mathbf{A} \odot \nabla \mathbf{X}$.

The min operator can be substituted with a sparse matrix M applied to the vectorized form of $|\nabla X|$ [59] satisfying

$$\mathbf{M}(x,z) = \begin{cases} 1, & z = \arg\min = |\nabla \mathbf{X}|(y) \\ 0, & \text{otherwise.} \end{cases} \tag{6}$$

Letting $\mathbf{D} = \mathbf{M} * \mathbf{A} * \nabla$, it yields the local minimum difference (LMD) operation as

$$\text{LMD}(\mathbf{X}) = \mathbf{DX}. \tag{7}$$

B. LMD

This section will define a novel regularization term in detail and explain its effectiveness. First, Fig. 1 is depicted to show that the local structural features of the image are destroyed due to the noise. It means that the LMD values of HSIs are disturbed by noise. To further clarify the phenomenon, the LMD is defined as follows:

$$\text{LMD}(\mathbf{X})(p) = \min_{q \in \mathcal{N}(p)} \nabla \mathbf{X}^b(q) \tag{8}$$

where p and q are pixel positions; $\text{LMD}(x)$ denotes an image patch centered at p; b represents the bth spectral band with $b \in \{1, \ldots, B\}$.

Next, the structural feature property of HSI is modeled. As shown in Fig. 2, it is observed that only a few singular values hold significance when the SVD operator is used to LMD. It indicates that LMD is an LR structure. It gets that the rank of the LMD of the original HSI $\mathbf{X}$ is smaller than the rank of the noisy HSI $\mathbf{Y}$. In the presence of noise in the image, it causes fluctuations or variations in the LMD matrix of the noisy image. In contrast, the clean image is not affected by noise. Consequently, it is concluded that the rank of the LMD matrix of the original HSI $\mathbf{X}$ is inevitably lower than that of the noisy HSI $\mathbf{Y}$. This finding emphasizes the inherent LR property of LMD and reflects its potential for capturing and preserving the characteristics of the structure in the denoising process. Therefore, we can use the nuclear norm to describe the correlation among these LMD matrices.

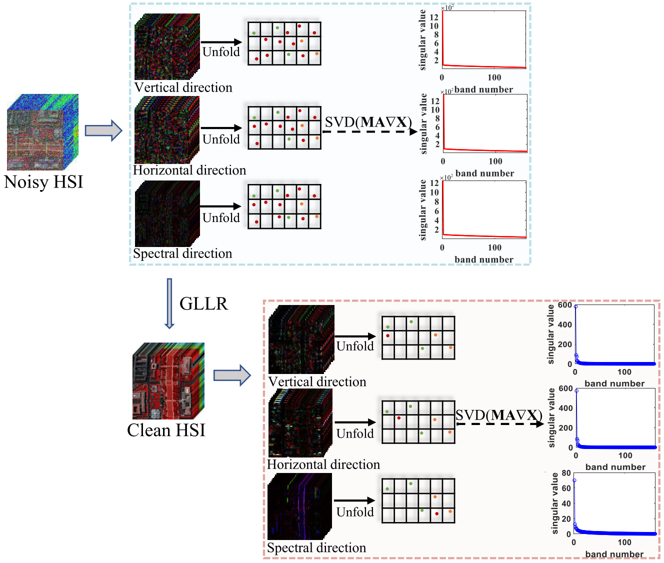

Fig. 2. LR prior of the LMD.

Then, it gets

$$\|\text{LMD}(\mathbf{X})\|_* = \|\mathbf{MA}\nabla\mathbf{X}\|_* \tag{9}$$

where $\mathbf{MA}\nabla\mathbf{X}$ builds upon $\nabla\mathbf{X}$ by the structural characteristics prior of HSI.

Fig. 3 shows how GLLR integrates both two priors to restore images. Next, we integrate $\|\text{LMD}(\mathbf{X})\|_*$ into (3) and propose the following HSI denoising model (10):

$$\begin{aligned} \min_{\mathbf{X},\mathbf{S}} \;& \|\text{LMD}(\mathbf{X})\|_* + \|\nabla\mathbf{X}\|_* + \lambda\|\mathbf{S}\|_1 \\ \text{s.t. } & \|\mathbf{Y} - \mathbf{X} - \mathbf{S}\|_F \leq \delta. \end{aligned} \tag{10}$$

C. LMD for HSI

To solve optimization model (10) using the augmented lagrange multiplier (ALM) method, the first step is to transform model (10) into the following equivalent model:

$$\begin{aligned} \min_{\mathbf{X},\mathbf{S},\mathbf{H},\mathbf{J}} \;& \sum_{i=1}^{3} \|\mathbf{H}_i\|_* + 3\lambda_1\|\mathbf{S}\|_1 + \sum_{i=1}^{3} \lambda_2 \|\mathbf{J}_i\|_* \\ \text{s.t. } & \|\mathbf{Y} - \mathbf{X} - \mathbf{S}\|_F^2 \leq \delta \\ & \nabla_i(\mathbf{X}) = \mathbf{H}_i \\ & \mathbf{J}_i = \mathbf{MA}\nabla_i(\mathbf{X}), \quad i = 1,2,3 \\ & \text{rank}(\mathbf{H}) \leq r_1, \quad \text{rank}(\mathbf{J}) \leq r_2 \end{aligned} \tag{11}$$

where $\mathbf{M}$ and $\mathbf{A}$ are the minimum and absolute value operators, respectively.

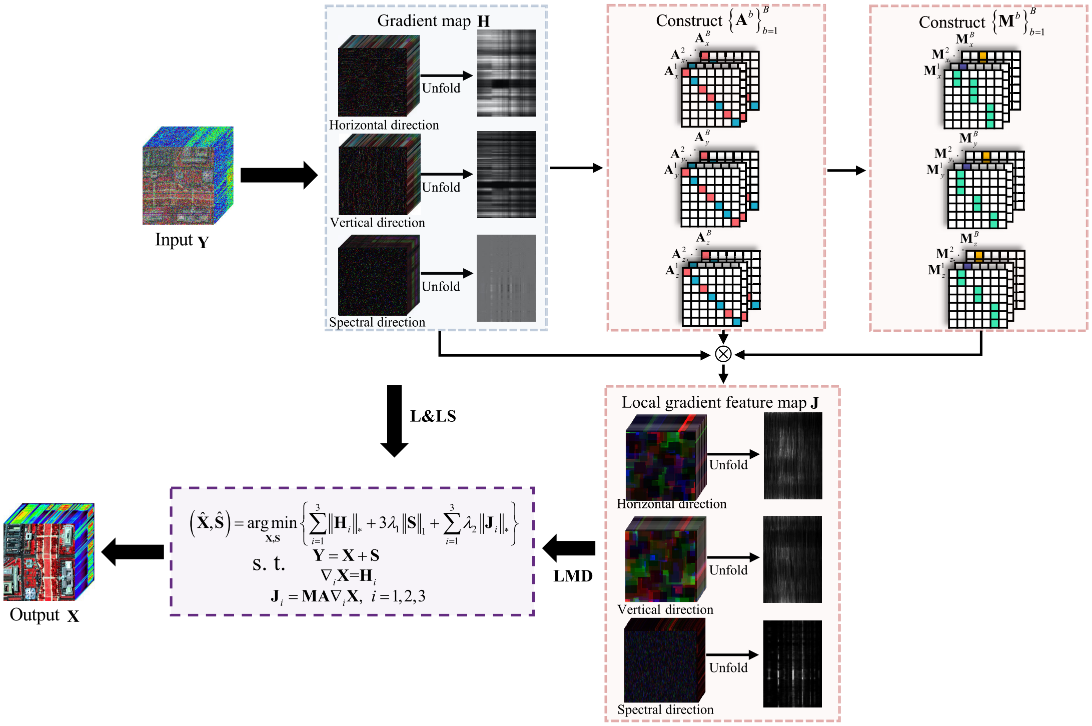

Fig. 3. Flowchart of the presented GLLR. $\otimes$ is the matrix product.

D. Derivation of Model Solving

The expression for the ALM of (11) is given as

$$\begin{aligned}
&\min \ell(\mathbf{X}, \mathbf{S}, \mathbf{H}, \mathbf{J}, \mathbf{\Gamma_i})\\
&= \min_{\mathbf{X},\mathbf{S},\mathbf{H},\mathbf{J},\mathbf{\Gamma}_i} \sum_{i=1}^{3} \|\mathbf{H}_i\|_* + 3\lambda_1 \|\mathbf{S}\|_1 + \sum_{i=1}^{3} \lambda_2 \|\mathbf{J}_i\|_*\\
&\quad + \langle \mathbf{\Gamma}_i, \nabla_i \mathbf{X} - \mathbf{H}_i \rangle + \langle \mathbf{\Gamma}, \mathbf{Y} - \mathbf{X} - \mathbf{S} \rangle\\
&\quad + \langle \mathbf{\Gamma}_i, \mathbf{D}_i \mathbf{X} - \mathbf{J}_i \rangle + \frac{\mu_1}{2} \|\mathbf{Y} - \mathbf{X} - \mathbf{S}\|_F^2\\
&\quad + \frac{\mu_2}{2} \sum_{i=1}^{3} \left(\|\nabla_i \mathbf{X} - \mathbf{H}_i\|_F^2 + \|\mathbf{D}_i \mathbf{X} - \mathbf{J}_i\|_F^2 \right)\\
&\quad \text{s.t. } \operatorname{rank}(\mathbf{H}) \le r_1, \quad \operatorname{rank}(\mathbf{J}) \le r_2
\end{aligned} \tag{12}$$

where λ is the regularization parameter, $\mathbf{\Gamma}$ is the lagrange multiplier, μ is penalty parameter, and $\langle , \rangle$ is the inner product of two matrices. The optimization problem in (12) can be solved by the following three subproblems:

$$\mathbf{H}^{t+1} = \arg\min_{\mathbf{H}} \sum_{i=1}^{3} \|\mathbf{H}_i\|_* + \frac{\mu_2}{2} \left\| \nabla_i \mathbf{X} - \mathbf{H}_i + \frac{\mathbf{\Gamma}_i}{\mu_2} \right\|_F^2 \tag{13}$$

$$\mathbf{S}^{t+1} = \arg\min_{\mathbf{S}} 3\lambda \|\mathbf{S}\|_1 + \frac{\mu_1}{2} \left\| \mathbf{Y} - \mathbf{X} - \mathbf{S} + \frac{\mathbf{\Gamma}_7}{\mu_1} \right\|_F^2 \tag{14}$$

$$\mathbf{J}^{t+1} = \arg\min_{\mathbf{J}} \sum_{i=1}^{3} \lambda_2 \|\mathbf{J}_i\|_* + \frac{\mu_2}{2} \left\| \mathbf{D}_i \mathbf{X} - \mathbf{J}_i + \frac{\mathbf{\Gamma}_{i+3}}{\mu_2} \right\|_F^2. \tag{15}$$

Next, the solving steps of each subproblem involving variables are presented as follows.

1) *Calculate* **H***:* By fixing other variables in (12), we can obtain for subproblem **H**

$$\begin{cases} \mathbf{H}_i^{t+1} = \mathbf{U}\mathcal{S}_{1/\mu_2}(\mathbf{\Sigma})\mathbf{V}^T \\ \mathbf{U\Sigma V}^T = \operatorname{svd}\left(\nabla_i \mathbf{X}^t + \mathbf{\Gamma}_i^t / \mu_2, \text{ `econ'}\right). \end{cases} \tag{16}$$

2) *Calculate* **S***:* The subproblem **S** related to (14) can be obtained by utilizing the soft threshold shrinkage operator [60]

$$\Re = \begin{cases} x - \delta, & \text{if } x > \delta \\ x + \delta, & \text{if } x < -\delta \\ 0, & \text{otherwise.} \end{cases} \tag{17}$$

Then the solution of subproblem **S** can be formulated as follows:

$$\mathbf{S}^{t+1} = \mathcal{S}_{3\lambda/\mu_1}\left(\mathbf{Y} - \mathbf{X}^{(t)} + \frac{\mathbf{\Gamma}_7}{\mu_1} \right). \tag{18}$$

3) *Calculate* **J***:* The optimization equation for solving the subproblem **J** can be solved similar to that of (16)

$$\begin{cases} \mathbf{J}_i^{t+1} = \mathbf{U}\mathcal{S}_{\lambda_2/\mu_2}(\mathbf{\Sigma})\mathbf{V}^T \\ \mathbf{U\Sigma V}^T = \operatorname{svd}\left(\mathbf{D}_i \mathbf{X}^t + \mathbf{\Gamma}_{i+3}^t / \mu_2, \text{ `econ'}\right). \end{cases} \tag{19}$$

4) *Calculate* **X***:* We can solve **X** given **H** and **J** in the following manner:

$$\begin{aligned}
\arg\min_{\mathbf{X}} &\sum_{i=1}^{3} \left(\frac{\mu_2}{2} \|\nabla_i \mathbf{X} - \mathbf{H}_i^{t+1} + \frac{\mathbf{\Gamma}_i}{\mu_2} \|_F^2 \right)\\
&+ \frac{\mu_1}{2} \left\| \mathbf{Y} - \mathbf{X} - \mathbf{S}^{t+1} + \frac{\mathbf{\Gamma}_7}{\mu_1} \right\|_F^2\\
&+ \sum_{i=1}^{3} \left(\frac{\mu_2}{2} \left\| \mathbf{D}_i \mathbf{X} - \mathbf{J}_i^{t+1} + \frac{\mathbf{\Gamma}_{i+3}}{\mu_2} \right\|_F^2 \right).
\end{aligned} \tag{20}$$

To deal with the large size of $\mathbf{H}$, we introduce another auxiliary variable, where $\mathbf{q} \rightarrow \mathbf{X}$, and (20) can be represented as

$$\begin{aligned}\arg\min_{\mathbf{X}}\ &\sum_{i=1}^{3}\left(\frac{\mu_2}{2}\left\|\nabla_i\mathbf{X}-\mathbf{H}_i^{t+1}+\frac{\mathbf{\Gamma}_i}{\mu_2}\right\|_F^2\right)\\ &+\frac{\mu_1}{2}\left\|\mathbf{Y}-\mathbf{X}-\mathbf{S}^{t+1}+\frac{\mathbf{\Gamma}_7}{\mu_1}\right\|_F^2+\frac{\mu_3}{2}\|\mathbf{q}-\mathbf{X}\|^2\\ &+\sum_{i=1}^{3}\left(\frac{\mu_2}{2}\left\|\mathbf{D}_i\mathbf{q}-\mathbf{J}_i^{t+1}+\frac{\mathbf{\Gamma}_{i+1}}{\mu_2}\right\|_F^2\right).\end{aligned}\tag{21}$$

The subproblems related to $\mathbf{X}$ and $\mathbf{q}$ can be updated using an alternative approach as follows:

$$\begin{aligned}\arg\min_{\mathbf{X}}\ &\sum_{i=1}^{3}\left(\frac{\mu_2}{2}\left\|\nabla_i\mathbf{X}-\mathbf{H}_i^{t+1}+\frac{\mathbf{\Gamma}_i}{\mu_2}\right\|_F^2\right)\\ &+\frac{\mu_1}{2}\left\|\mathbf{Y}-\mathbf{X}-\mathbf{S}^{t+1}+\frac{\mathbf{\Gamma}_7}{\mu_1}\right\|_F^2+\frac{\mu_3}{2}\|\mathbf{q}-\mathbf{X}\|^2\end{aligned}\tag{22}$$

$$\begin{aligned}\arg\min_{\mathbf{q}}\ &\sum_{i=1}^{3}\left(\frac{\mu_2}{2}\left\|\mathbf{D}_i\mathbf{q}-\mathbf{J}_i^{t+1}+\frac{\mathbf{\Gamma}_{i+1}}{\mu_2}\right\|_F^2\right)\\ &+\frac{\mu_3}{2}\|\mathbf{q}-\mathbf{X}\|^2.\end{aligned}\tag{23}$$

The problem (22) can be optimized by solving it in the following manner:

$$\begin{aligned}&\left[\mu_2\sum_{i=1}^{3}\nabla_i^T\nabla_i+(\mu_1+\mu_3)\mathbf{I}\right]\mathbf{X}\\ &\quad=\nabla_i^T\left(\mu_2\sum_{i=1}^{3}\mathbf{H}_i^{t+1}-\mathbf{\Gamma}_i^{t+1}\right)+\mu_1\left(\mathbf{Y}-\mathbf{S}^{t+1}\right)\\ &\qquad+\mathbf{\Gamma}_7^{t+1}+\mu_3\mathbf{q}^t\end{aligned}\tag{24}$$

where ∇^T denotes the transpose operator of ∇. By executing Fourier transform on both sides of (24), using the convolution theorem [61], the solution of $\mathbf{X}_{t+1}$ is given by the following formula:

$$\begin{cases}\mathbf{T}_x=|\mathcal{F}(\mathbf{D}_1)|^2+\mathcal{F}(\mathbf{D}_2)|^2+|\mathcal{F}(\mathbf{D}_3)|^2\\ \mathbf{F}=\displaystyle\sum_{n=1}^{3}\mathcal{F}(\mathbf{D}_n)^*\odot\mathcal{F}\left(\mathrm{fold}\left(\mu_2\mathbf{F}_i^{t+1}-\mathbf{\Gamma}_i^t\right)\right)\\ \mathbf{X}^{t+1}\\ \quad=\mathcal{F}^{-1}\left(\dfrac{\mathcal{F}\left(\mathrm{fold}\left(\mu_1(\mathbf{Y}-\mathbf{S}^{t+1})+\mathbf{\Gamma}_7^t+\mu_3\mathbf{q}^{t+1}\right)\right)+\mathbf{H}}{(\mu_1+\mu_3)\mathbf{I}+\mu_2\mathbf{T}_x}\right).\end{cases}\tag{25}$$

The solution of $\mathbf{q}$-related problem is obtained by

$$\mathbf{q}=\frac{\mathbf{D}_i^T\left(\mu_2\mathbf{J}_i^{t+1}-\mathbf{\Gamma}_{i+3}\right)+\mu_3\mathbf{X}^{t+1}}{\mu_2\mathbf{D}_i^T\mathbf{D}_i+\mu_3\mathbf{I}}.\tag{26}$$

5) *Computing Multipliers* $\mathbf{\Gamma}$*:*

$$\begin{cases}\mathbf{\Gamma}_i^{t+1}=\mathbf{\Gamma}_i^t+\mu\left(\nabla_i\mathbf{X}^{t+1}-\mathbf{H}_i^{t+1}\right), & i=1,2,3\\ \mathbf{\Gamma}_{i+3}^{t+1}=\mathbf{\Gamma}_{i+3}^t+\mu\left(\mathbf{D}_i\mathbf{X}^{t+1}-\mathbf{J}^{t+1}\right), & i=1,2,3\\ \mathbf{\Gamma}_7^{t+1}=\mathbf{\Gamma}_7^t+\mu\left(\mathbf{Y}-\mathbf{X}^{t+1}-\mathbf{S}^{t+1}\right), & \mu=\mu\rho\end{cases}\tag{27}$$

where ρ denotes a constant.

E. Algorithm Description

Algorithm 1 summarizes the main steps of optimizing and solving the HSI denoising method based on GLLR.

Algorithm 1 GLLR-Based HSI Denoising

```
Input: Obseverd image $\mathbf{Y}$, $\epsilon_1 = \epsilon_2 = \epsilon_3 = 10^{-6}$ and $\lambda_1 = 5/\sqrt{hw}$.
Initialization: $\mathbf{S} = \mathbf{0}$, $\mathbf{X} = \mathrm{randn}(hw, b)$
  while not converge do
    Upadate $\mathbf{H}_i^{t+1}$ by (16)
    Upadate $\mathbf{J}_i^{t+1}$ by (19)
    Upadate $\mathbf{q}^{t+1}$ by (23)
    Upadate $\mathbf{X}^{t+1}$ by (25)
    Upadate $\mathbf{S}^{t+1}$ by (18)
    Upadate $\mathbf{\Gamma}_i^{t+1}$ by (27)
    $\mu = \rho\mu$, $t := t + 1$
    judge the convergence conditions
      $\|\mathbf{Y} - \mathbf{X}^{t+1} - \mathbf{S}^{t+1}\|_F^2/\|\mathbf{Y}\|_F^2 \leq \epsilon_1$
      $\|\nabla_i\mathbf{X}^{t+1} - \mathbf{H}_i^{t+1}\|_F^2/\|\mathbf{Y}\|_F^2 \leq \epsilon_2$, $i = 1, 2, 3$
      $\|\mathbf{D}_i\mathbf{X}^{t+1} - \mathbf{J}_i^{t+1}\|_F^2/\|\mathbf{Y}\|_F^2 \leq \epsilon_3$, $i = 1, 2, 3$
  end while
Output: The restoration result $\mathbf{X}$.
```

IV. EXPERIMENT ANALYSIS

This section introduces the evaluation metrics, experimental setups, and test data used in the experiment. The comparative experiments on multiple data are implemented to evaluate the effectiveness and superiority of the proposed denoising method.

To thoroughly illustrate the superiority of the presented GLLR method, the model-based and DL-based denoising methods are selected as competitors. In detail, the model-based methods includes LRTV [35], LRMR [35], CTV-RPCA [43], principal component pursuit (PCP) [62], tensor dictionary learning (TDL) [63], and non-local meets global (NGMeet) [64]. The DL-based methods have single denoising CNN (SdeCNN) [45], global reasoning network (GRN-Net) [49], and subspace-based multidimensional sparse network (SMDS-Net) [50]. In order to ensure the fairness of the experiments, the parameters of all comparison methods are finetuned to achieve optimal performance based on the default settings of the code from the author's website or the range of parameter settings in the article.

Benchmark Dataset: Herein, two simulation data of HSIs are employed to demonstrate the effectiveness of the developed GLLR framework for HSI denoising. The first data are the Washington D.C. Mall data consisting of 191 bands with the wavelength from 401 to 2473 nm obtained from the HYDICE sensor after discarding vapor absorption bands. According to literature [43], the simulation experiments are performed using data of size 200 × 200 × 160 [regions in spatially: (567:766, 40:239)]. The second dataset is the Pavia city center data acquired by the reflective optics system imaging spectrometer. Note that the front few bands of the Pavia city center data contaminants heavy noise and cannot be selected for comparison references of noise removal experiments. From [19], we removed the corresponding noise-disturbed

TABLE I
PERFORMANCE COMPARISON ON W.DC MALL

Case	Index	Noisy	SdeCNN	SMDS-Net	GRN-Net	TDL	LRMR	PCP	LRTV	NGMeet	CTV-RPCA	Proposed
Case 1	PSNR	19.48	33.23	32.56	22.98	23.28	33.93	31.68	33.89	34.23	34.23	**34.97**
	SSIM	0.500	0.949	0.940	0.789	0.680	0.959	0.958	0.966	0.964	0.961	**0.967**
	SAM	31.69	6.07	7.16	18.15	19.70	6.20	6.47	5.64	5.70	5.57	**5.34**
	ERGAS	458.55	77.65	85.81	307.20	272.30	71.73	99.42	74.31	73.78	69.50	**63.83**
	Time/s	-	**7.53**	24.70	9.44	26.62	26.62	26.62	26.62	80.36	80.36	1254.87
Case 2	PSNR	14.53	26.78	27.31	23.21	24.00	44.17	45.12	36.82	28.16	**49.69**	48.82
	SSIM	0.354	0.867	0.887	0.776	0.880	0.995	0.998	0.985	0.914	**0.998**	0.998
	SAM	36.80	8.50	8.49	18.71	8.69	2.33	1.28	2.92	7.30	**0.91**	1.16
	ERGAS	693.14	172.62	144.33	306.86	240.98	23.76	26.67	62.59	145.62	15.25	**14.58**
	Time/s	-	**7.45**	18.51	9.27	16.92	139.01	17.48	139.05	77.36	89.47	1504.79
Case 3	PSNR	13.45	26.51	26.83	23.17	23.79	33.63	31.32	33.35	27.99	33.45	**34.73**
	SSIM	0.272	0.856	0.868	0.774	0.862	0.955	0.951	0.960	0.911	0.954	**0.963**
	SAM	40.10	8.95	9.02	18.83	9.63	6.18	6.63	5.68	7.47	5.77	**5.36**
	ERGAS	780.58	176.79	151.78	307.75	244.95	73.37	96.73	78.59	147.12	75.68	**65.34**
	Time/s	-	**7.57**	27.15	9.39	16.10	146.01	15.51	148.53	79.18	162.06	1658.96
Case 4	PSNR	21.77	34.98	35.95	24.01	29.07	35.90	33.68	36.01	**37.26**	35.43	36.87
	SSIM	0.606	0.967	0.972	0.780	0.911	0.974	0.972	0.972	**0.982**	0.971	0.977
	SAM	23.47	5.11	5.09	17.41	7.70	5.11	5.47	5.22	**3.79**	4.94	4.50
	ERGAS	299.77	64.59	58.93	258.52	134.74	57.78	75.83	57.55	**49.37**	60.88	51.58
	Time/s	-	7.40	24.88	10.20	15.10	150.77	14.48	137.17	76.94	154.78	1183.13
Case 5	PSNR	13.83	25.49	26.04	23.23	23.56	35.31	33.02	34.32	26.63	34.97	**36.23**
	SSIM	0.292	0.835	0.876	0.713	0.847	0.969	0.967	0.970	0.882	0.967	**0.973**
	SAM	38.69	9.90	8.55	19.43	10.90	5.16	5.56	5.33	8.92	5.02	**4.58**
	ERGAS	758.23	205.09	165.17	277.73	264.03	60.93	81.35	72.00	181.89	64.21	**55.44**
	Time/s	-	**7.38**	24.88	9.89	23.30	145.38	14.90	139.13	81.19	165.88	1401.62
Case 6	PSNR	13.45	26.67	27.08	23.12	24.13	33.26	31.0	33.40	28.23	33.32	**34.68**
	SSIM	0.270	0.855	0.870	0.771	0.867	0.953	0.950	0.962	0.912	0.953	**0.962**
	SAM	40.21	8.78	8.88	18.92	9.16	6.31	6.60	5.79	7.20	5.79	**5.37**
	ERGAS	779.16	171.65	147.71	308.40	232.09	77.13	99.42	78.54	141.31	76.69	**65.51**
	Time/s	-	**7.48**	27.15	9.14	14.62	144.86	6.60	6.60	80.62	6.60	1158.89

bands and selected a subimage with a size of 200 × 200 × 85 [regions in spatially: (1:200, 25:224)]. In this section, we set the following six noise degradation cases.

Evaluation Metrics and Experiment Setup:

1) In Case 1, each band of the HSI is corrupted by Gaussian noise at different levels, where the variance of the Gaussian noise is randomly generated from [0.05–0.1].
2) In Case 2, all bands of two HSIs are corrupted by salt-and-pepper noise with a proportion of 0.1.
3) In Case 3, Gaussian noise with standard variance 0.1 and salt-and-pepper noise with proportion 0.1 are simulated to generate degraded images.
4) In Case 4, the same level of Gaussian noise as in Case 1 is added, additionally, 40% of the bands are contaminated by stripe noise.
5) In Case 5, the same level of Gaussian noise as in Case 1 is applied to simulate a Gaussian noise scenario. Moreover, salt-and-pepper noise with proportions ranging from [0.05–0.15] is added to both HSIs.
6) In Case 6, the same levels of Gaussian and salt-and-pepper noise as in Case 3 are simulated and the stripe noise same as Case 4 are added simultaneously.

The quality of HSI reflects in two aspects, i.e., spatial quality and spectral quality. Peak signal-to-noise ratio (PSNR) and structural similarity (SSIM) are usually used to evaluate the spatial quality of HSI. The larger the values of PSNR and SSIM, the better the restoration quality of HSI. Erreur relative global adimensionnelle de synthèse (ERGAS) and spectral angle mapper (SAM) are utilized to evaluate the spectral quality of HSI. The smaller the ERGAS and SAM value, the better the quality of the recovered HSI. Therefore, PSNR, SSIM, SAM, and ERGAS are employed to evaluate the experiment results using the proposed GLLR method and above competitors.

A. Simulation Experiments

Tables I and II list the quantitative evaluation results of six degradation cases using our method and other comparison methods for Washington D.C. Mall and Pavia City datasets, respectively. For the convenience of finding, the best result and the second-best result of each evaluation metric in Tables I and II are highlighted in bold and underlined, respectively. Figs. 4 and 5, respectively, display the comparative experiment results of synthetic false-color images of the Washington D.C. Mall under Case 1 and the Pavia

TABLE II
PERFORMANCE COMPARISON ON PAVIA CITY

Case	Index	Noisy	SdeCNN	SMDS-Net	GRN-Net	TDL	LRMR	PCP	LRTV	NGMeet	CTV-RPCA	Proposed
Case 1	PSNR	19.67	35.13	31.89	28.56	23.38	33.97	31.46	34.82	35.03	34.76	**35.15**
	SSIM	0.380	0.948	0.880	0.879	0.620	0.932	0.925	0.934	0.950	0.947	**0.950**
	SAM	39.14	5.55	10.09	5.55	21.61	6.83	7.30	7.30	9.40	5.51	**5.07**
	ERGAS	493.24	**69.36**	102.92	181.98	285.66	81.17	108.52	74.92	74.48	73.43	70.29
	Time/s	-	**3.72**	9.44	9.44	13.66	118.96	6.23	29.90	73.41	29.90	1314.2
Case 2	PSNR	14.32	26.81	26.41	27.46	20.95	44.86	45.04	38.41	27.92	44.97	**50.25**
	SSIM	0.242	0.841	0.801	0.859	0.805	0.993	0.998	0.966	0.884	0.998	**0.999**
	SAM	42.75	7.42	12.47	9.23	8.11	2.43	**1.06**	5.79	6.32	**1.06**	1.37
	ERGAS	784.13	187.01	175.26	199.26	366.32	23.96	26.43	85.60	165.08	25.68	**12.47**
	Time/s	-	**3.71**	8.58	7.24	8.67	101.46	6.83	40.45	69.23	65.74	917.09
Case 3	PSNR	13.28	26.69	25.93	27.42	18.91	33.28	30.52	33.10	27.85	33.87	**34.72**
	SSIM	0.165	0.830	0.769	0.855	0.748	0.916	0.907	0.929	0.880	0.934	**0.937**
	SAM	46.66	7.57	9.87	12.7	8.24	7.30	7.72	7.37	6.413	5.83	**5.81**
	ERGAS	881.47	188.76	184.19	200.34	458.21	87.08	118.85	98.81	166.04	82.91	**74.21**
	Time/s	-	**3.60**	8.74	7.26	7.95	119.41	6.22	38.11	72.20	52.30	803.00
Case 4	PSNR	21.82	36.78	36.10	28.47	28.46	35.70	32.99	36.79	**37.49**	35.35	36.82
	SSIM	0.476	0.961	0.953	0.896	0.866	0.951	0.9420	0.957	**0.962**	0.952	**0.962**
	SAM	30.23	5.13	6.09	8.08	9.69	6.01	6.01	5.42	6.13	5.53	**4.87**
	ERGAS	331.62	60.22	65.50	212.25	157.04	66.90	92.21	**58.86**	63.59	70.48	58.90
	Time/s	-	**3.60**	10.75	10.20	12.83	102.56	6.47	30.61	67.98	63.30	723.01
Case 5	PSNR	13.73	25.62	26.19	24.54	21.17	34.80	31.85	33.96	26.22	34.84	**36.13**
	SSIM	0.185	0.804	0.845	0.816	0.769	0.942	0.932	0.941	0.809	0.945	**0.953**
	SAM	44.57	8.47	8.83	8.08	9.46	5.75	6.61	6.99	9.74	5.65	**4.96**
	ERGAS	847.55	218.43	180.86	266.41	362.00	73.64	104.93	94.20	219.61	74.71	**63.65**
	Time/s	-	**3.73**	8.85	9.89	10.35	119.86	6.24	39.03	78.41	65.28	742.00
Case 6	PSNR	13.28	26.84	26.00	27.42	20.87	33.01	30.16	33.30	28.03	33.78	**34.63**
	SSIM	0.164	0.828	0.769	0.854	0.788	0.921	0.906	0.929	0.880	0.934	**0.936**
	SAM	46.94	7.56	10.10	12.77	7.45	6.82	7.91	7.52	6.56	6.02	**5.88**
	ERGAS	880.10	185.02	183.47	200.89	363.93	87.77	126.90	100.08	162.37	83.83	**75.12**
	Time/s	-	**3.67**	8.67	7.30	7.67	91.85	6.36	39.62	71.38	64.59	890.53

City under Case 6. For the Washington D.C. Mall under Case 1, the corresponding bands of red, green, and blue are 58, 27, and 17. For the Pavia City under Case 6, the corresponding bands of red, green, and blue are 75, 50, and 10. To clearly display the recovery performance, we magnify the local details of each subfigure in Fig. 4. From Fig. 4, TDL and SMDS-Net in contrast to other methods are less effective in removing the complex noise under Case 1. SdeCNN and GRN-Net display better denoising performance but smooth out image details. The denoising results using LRMR and PCP are visually good, but there is still a slight noise residue. In general, CTV-RPCA, LRTV, NGMeet, and the proposed method achieve a good balance between denoising and structure retention. From Table I, it follows that GRN-Net has weak mining capability for the feature of HSI with more spectral information. For Cases 1, 3, 5, and 6, the developed GLLR shows the best performance. In Case 2, the developed GLLR gets the best value of ERGAS and the second-best values of PSNR, SSIM, and SAM behind CTV-RPCA. For Case 4, NGMeet and the proposed method obtain the best value and the second-best value, respectively. According to Fig. 5, the proposed GLLR method also shows excellent performance visually. In Table II, the proposed method obtains the best metrics under Cases 1, 2, 3, 5, and 6. NGMeet achieves the highest PSNR under Case 4. It yields that the presented GLLR is superior in terms of removing mixed noises. Based on quantitative evaluation results in Tables I and II, it is concluded that the proposed method is capable of removing multiple mixed noises and restoring the structure of HSI. In addition, the proposed LMD term is an effective compensation strategy because the proposed GLLR is superior over LRTV and CTV-RPCA according to Table II.

In addition, the recovery of spectral information is quite important for HSI denoising. With the Pavia data under Case 6, Fig. 6 plots the recovery spectral curves using different methods at the spatial location (178, 174). The clean spectral curve is also depicted in Fig. 6 to facilitate comparison. From Fig. 6(a)–(k), it follows that the proposed method has a superior ability to preserve spectral information in contrast to other competitors. It again verifies the effectiveness of the proposed GLLR method.

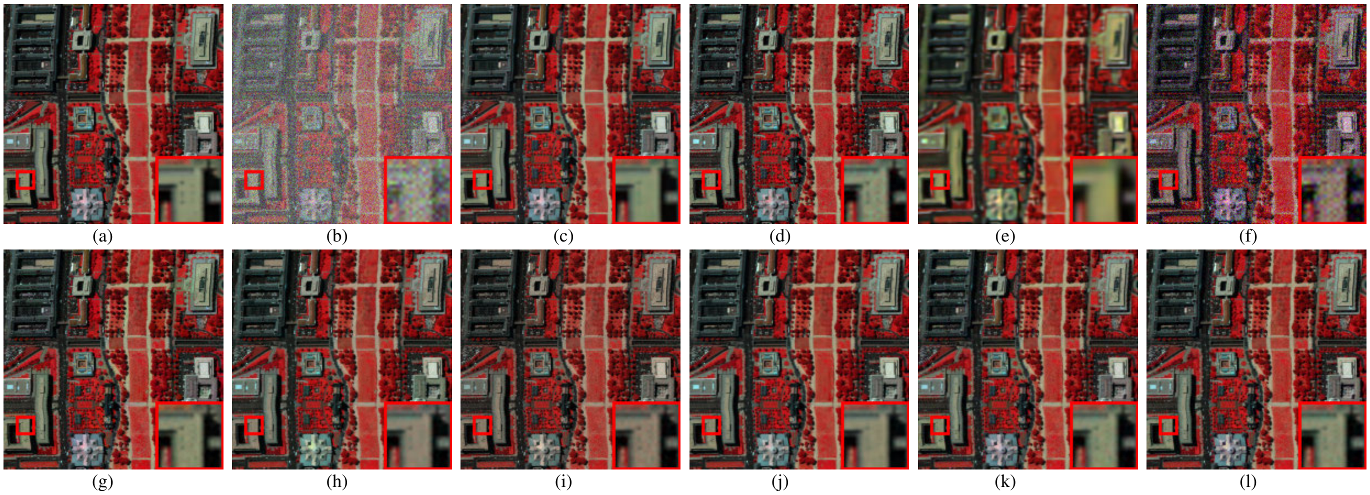

Fig. 4. Visual examples of restoration results in Case 1 (false-color: R for band 58, G for band 27, and B for band 17). (a) Original. (b) Noisy. (c) SdeCNN. (d) SMDS-Net. (e) GRN-Net. (f) TDL. (g) LRMR. (h) LRTV. (i) PCP. (j) NGMeet. (k) CTV-RPCA. (l) Proposed.

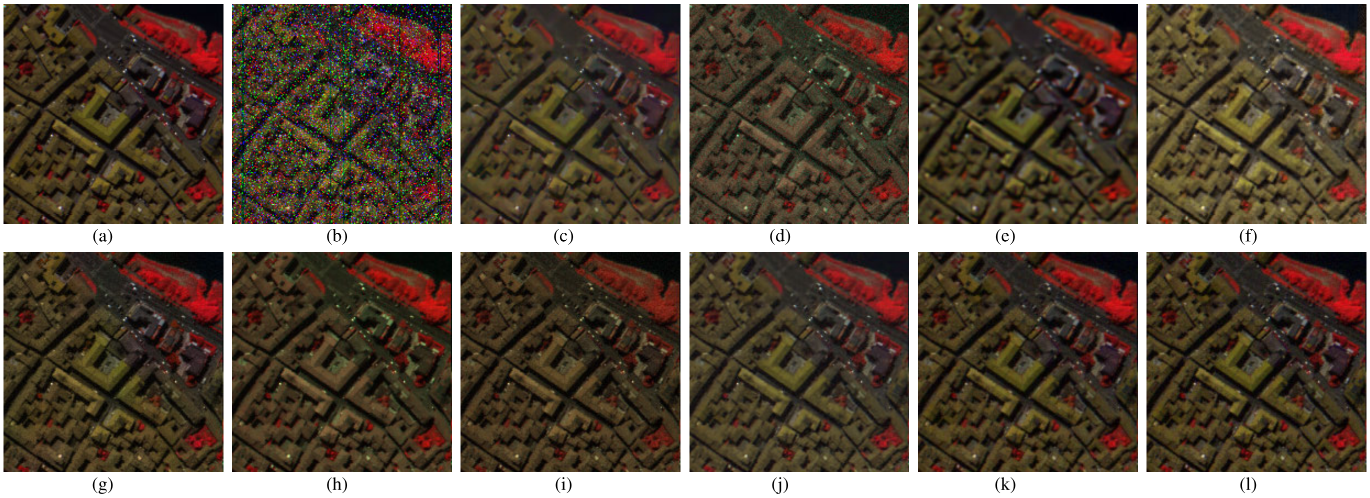

Fig. 5. Visual examples of restoration results in Case 6 (false-color: R for band 75, G for band 50, and B for band 10). (a) Original. (b) Noisy. (c) SdeCNN. (d) SMDS-Net. (e) GRN-Net. (f) TDL. (g) LRMR. (h) LRTV. (i) PCP. (j) NGMeet. (k) CTV-RPCA. (l) Proposed.

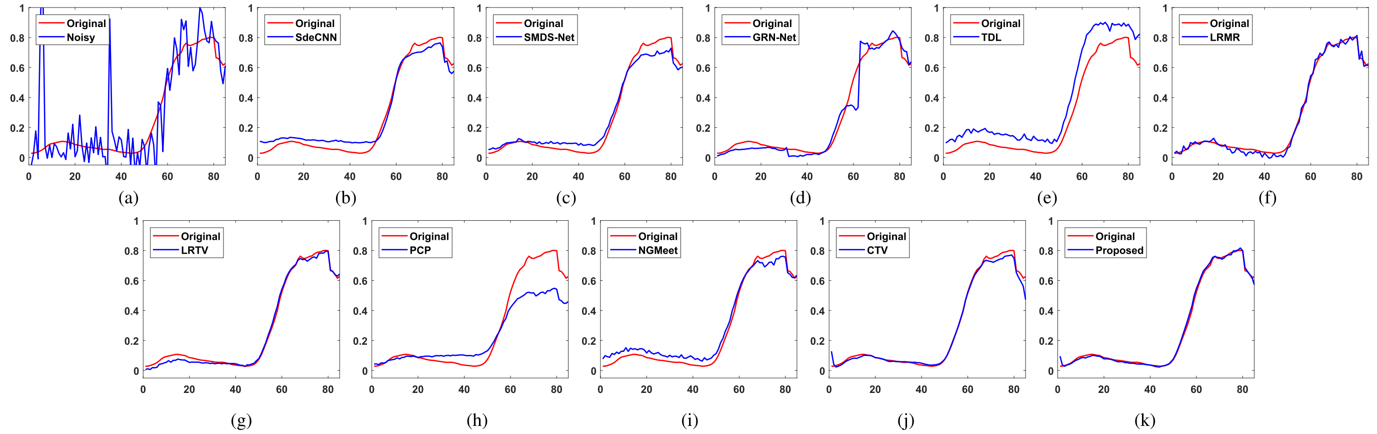

Fig. 6. Spectral curves in (178,174) of Pavia in Case 6. (a) Noisy. (b) SdeCNN. (c) SMDS-Net. (d) GRN-Net. (e) TDL. (f) LRMR. (g) LRTV. (h) PCP. (i) NGMeet. (j) CTV-RPCA. (k) Proposed.

B. Real Data Experiments

To further verify the reliability and compatibility of the proposed method, our experiments are conducted on two real-world noisy HSIs, i.e., the Urban data and the Indian Pines data. The Urban data is an image of size (307 × 307 × 210) obtained by the Hydice sensor. To subsequently process and analyze, we selected 188 bands by removing the water absorption bands from the original data of 210 bands.

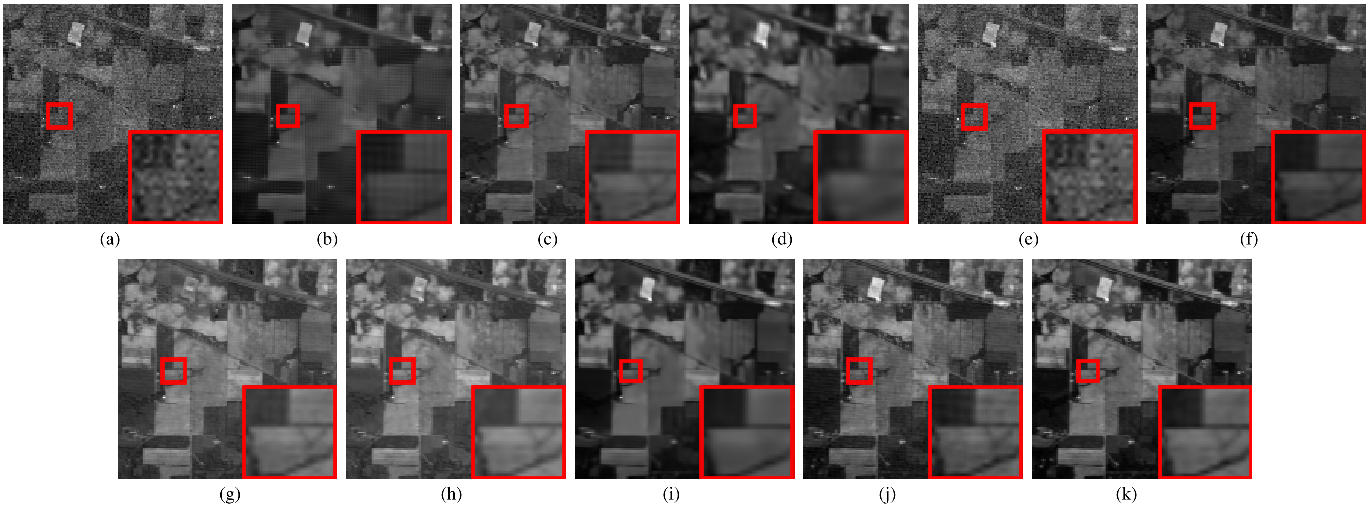
(a) (b) (c) (d) (e) (f) (g) (h) (i) (j) (k)

Fig. 7. Visual examples of restoration results on Indian Pines (band 2). (a) Noisy. (b) SdeCNN. (c) SMDS-Net. (d) GRN-Net. (e) TDL. (f) LRMR. (g) PCP. (h) LRTV. (i) NGMeet. (j) CTV-RPCA. (k) Proposed.

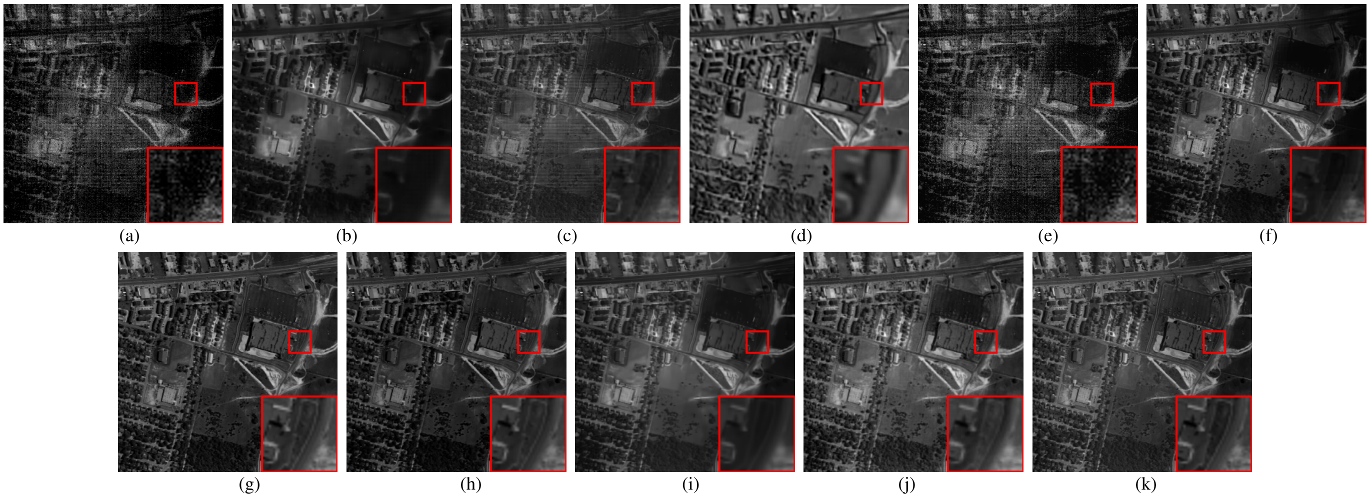
(a) (b) (c) (d) (e) (f) (g) (h) (i) (j) (k)

Fig. 8. Visual examples of restoration results on Urban (band 104). (a) Noisy. (b) SdeCNN. (c) SMDS-Net. (d) GRN-Net. (e) TDL. (f) LRMR. (g) PCP. (h) LRTV. (i) NGMeet. (j) CTV-RPCA. (k) Proposed.

From [10], we use the size (145 × 145 × 206) in the Indian Pines data captured by the AVIRIS sensor in Indian. It is noticed that there are significant differences in spatial, and spectral resolutions, practical scenarios, and noise intensity and types between the Urban data and the Indian Pine data. In the Urban data, band 104 is disturbed by mixed noise including random noise and stripe noise. In the Indian Pines data, band 2 is primarily affected by impulse noise. Therefore, these bands are chosen for qualitative evaluation experiments, and the corresponding results are shown in Figs. 7 and 8.

1) Indian Pines Dataset: Fig. 7 shows the denoising results for Indian pines, where impulse noise is predominantly present in this HSI. It can be seen that all methods have a denoising effect on noisy bands in different degrees. However, TDL has observable noise residues, GRN-Net, LRTV, SMDS-Net, and NGMeet have removed the noise from the HSI, but smooth the structure to varying degrees. In addition, SdeCNN has obvious artifacts that lead to data distortion. Slight residual noise exists in LRMR and PCP. CTV-RPCA and the proposed method achieve reliable results.

2) Urban Dataset: Unlike Indian pines, Urban data is corrupted by Gaussian noise and stripe noise. Fig. 8(e) shows that TDL still has obvious noise. SMDS removes the noise point in the HSI, but there are residue stripes. The intrinsic structural features of the HSI have been erased in Fig. 8(b)–(d). As can be seen from Fig. 8(f)–(k), LRMR, PCP, LRTV, NGmeet, CTV-RPCA, and GLLR can remove the mixed noise formed by the real stripe noise and Gaussian noise. Furthermore, to intuitively analyze the details of the recovery results by different methods, we have enlarged the local. The restoration results of LRMR, NGMeet, and CTV-RPCA have a loss of details. In contrast, PCP, LRTV, and GLLR effectively remove impulse noise and are equally outstanding in spatial texture preservation.

The recovery results of two real-scene HSIs with different resolutions, spatial distribution structures, and noises illustrate the reliability of the proposed GLLR in mixed noise removal, to some extent.

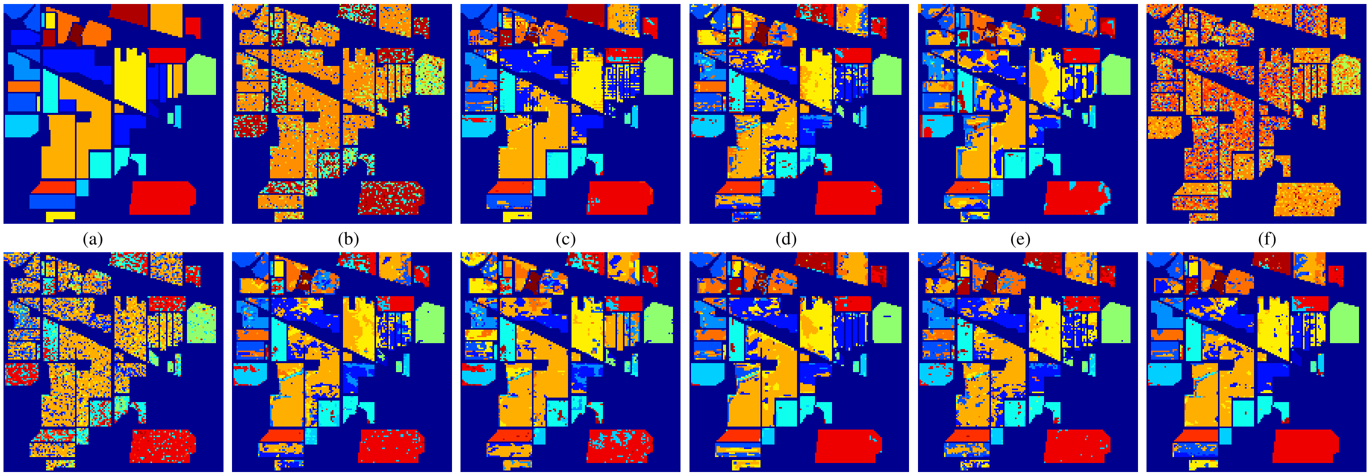
(a) (b) (c) (d) (e) (f)

(g) (h) (i) (j) (k) (l)

Fig. 9. HSI classification results for Indian Pines data before and after HSI denoising. The first eight bands with the lowest information entropy of Indian Pines. (a) Ground truth. (b) Noisy. (c) SdeCNN. (d) SMDS-Net. (e) GRN-Net. (f) TDL. (g) LRMR. (h) PCP. (i) LRTV. (j) NGMeet. (k) CTV-RPCA. (l) proposed.

TABLE III

CLASSIFICATION ACCURACY FOR THE FIRST EIGHT BANDS WITH LOWEST INFORMATION ENTROPY OF INDIAN PINES

Index	Noisy	SdeCNN	SMDS-Net	GRN-Net	TDL	LRMR	PCP	LRTV	NGMeet	CTV-RPCA	Proposed
OA	39.02%	80.84%	68.88%	62.65%	12.37%	41.83%	66.62%	61.73%	75.99%	74.47%	**81.59%**
Kappa	0.2377	0.7757	0.6378	0.5647	0.0414	0.3004	0.6083	0.5485	0.7197	0.7016	**0.7845**

C. Classification Results

To further analyze the performance of the proposed denoising method, the classification results with and without denoising are provided in this part. The support vector machine (SVM) is utilized to classify all recovery results of Indian Pines in the same environments, and overall accuracy (OA) and Kappa coefficient are used as evaluation metrics to quantitatively evaluate the classification. We selected the front eight bands with the lowest information entropy and randomly sampled 30% of the training samples. In Fig. 9, 16 land-cover classes are used to validate the classification accuracy. Fig. 9(b) and (c)–(l) give the classification results with and without denoising, respectively. Furthermore, the quantitative evaluation results of the classification are presented in Table III. It can be observed that almost all OA and Kappa coefficients of HSIs by denoising have been improved in contrast to the original noisy HSI. It indicates that the denoising process of HSIs is effective and significant. From Table III, the proposed GLLR method obtains the highest OA and Kappa coefficient, which reflects the superiority of the proposed HSI denoising method.

D. Discussion

Section IV-A and IV-B have provided the results of simulation and real data experiments. In this section, we further analyzed the impact of the variations of parameters λ_1 and λ_2 on HSI denoising results. The parameter r_1 can be estimated in two ways [19]: the Hysime [65] method and the observation method. The optimal value of desired rank becomes small as the noise level increases. The parameter r_2 is usually adjusted in a manual way. Various values of parameters λ_1 and λ_2 are employed to test the proposed denoising method.

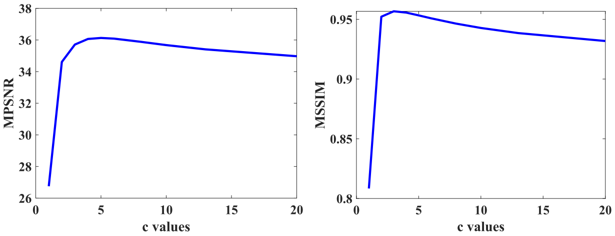

(a) (b)

Fig. 10. Sensitivity analysis of parameter λ_1 (c from 1 to 20 with $\lambda_1 = c(MN)^{1/2}$). (a) Change in the MPSNR value. (b) Change in the MSSIM value.

1) Sensitivity Analysis of Parameter λ_1: λ_1 is the regularization parameter affecting the denoising performance of HSI. The value of λ_1 can be changed by $\lambda_1 = c/(MN)^{1/2}$ where c comes from the set $\{1, 2, 3, 4, 5, 6, 8, 10, 13, 20\}$. Fig. 10 depicts the curves of MPSNR and MSSIM using the GLLR solver. It gets that MPSNR and MSSIM values are relatively stable as c changes from 3 to 20. Therefore, c is set as a fixed value $c = 5$ to ensure acceptable denoising results.

2) Sensitivity Analysis of Parameter λ_2: The value of λ_2 is selected from the set $\{0.0001, 0.0004, 0.001, 0.004, 0.007, 0.01, 0.02, 0.03\}$. In Fig. 11, the variations in MPSNR and MSSIM values are given with respect to different values of the parameter λ_2 using the GLLR solver. From Fig. 11, it yields that the proposed method achieves the optimal MPSNR value when $\lambda_2 \approx 0.02$.

In this article, the parameter selection of experiments on unknown real data employs the principle based on the

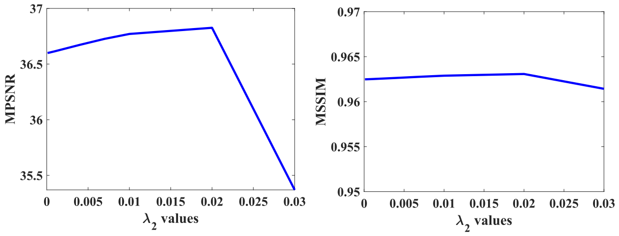

(a) (b)

Fig. 11. Sensitivity analysis of parameter λ_2. (a) Change in the MPSNR value. (b) Change in the MSSIM value.

TABLE IV

ABLATION EXPERIMENT

Index	CTV	Without LMD	With LMD
PSNR	34.84	35.11	**36.13**
SSIM	0.946	0.949	**0.953**
SAM	5.65	5.52	**4.96**
ERGAS	74.71	72.53	**63.65**

above-mentioned analysis results. Herein, it takes the parameter c as an example for illustration. According to Fig. 10, the values of MPSNR and MSSIM remain relatively stable for $c \in [3, 20]$. Therefore, c is selected to 5 for real data to ensure an acceptable result. Then, the parameter λ_1 can be set by $\lambda_1 = c/(MN)^{1/2}$. Similar to λ_1, the selections of λ_2 and rank can also be determined from Fig. 11 under the same principle.

3) Ablation Experiment: In this article, the proposed GLLR method integrates the local structural LR prior with the global TV LR prior. To demonstrate the significance of the proposed LMD, this part conducts an ablation experiment with and without the LMD term in the simulation experiment (Pavia data, Case 5). Thus, the following objective function (28) is formulated and solved using an iterative optimization algorithm based on the ALM technique:

$$\begin{aligned} \min_{\mathbf{X},\mathbf{S},\mathbf{H},\mathbf{J}} \ & \sum_{i=1}^{3} \|\mathbf{H}_i\|_* + 3\lambda_1 \|\mathbf{S}\|_1 \\ \text{s.t. } & \|\mathbf{Y} - \mathbf{X} - \mathbf{S}\|_F^2 \leq \delta \\ & \nabla_i(\mathbf{X}) = \mathbf{H}_i \\ & \text{rank}(\mathbf{H}) \leq r_1. \end{aligned} \tag{28}$$

The results of designed ablation experiment are listed in Table IV, where "Without LMD" represents the method with only the CTV regularization term and the same solution method as the proposed method is used. "CTV" refers to the correlation TV model based on the RPCA model proposed in [43]. From Table IV, the resulting results affirm the effectiveness of the proposed LMD regularization term.

E. Convergence Analysis

In this section, two cases, Case 5 and Case 6 of Pavia City, are provided to demonstrate the numerical convergence of the proposed algorithm. Fig. 12 plots the curves of the average PSNR and SSIM for Case 5 and Case 6 with respect to the iteration count of the developed GLLR solver. The average PSNR and SSIM values converge to steady values as the number of iterations increases. It verifies the convergence of the designed iterative optimization strategy to solve the GLLR model.

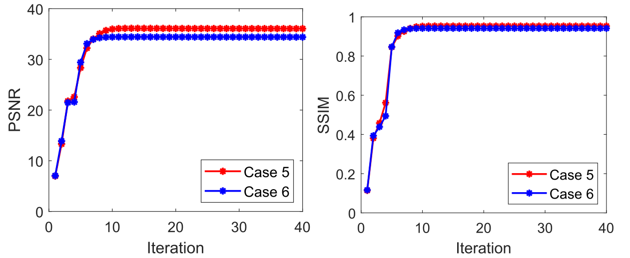

Fig. 12. Average PSNR and SSIM value curves in terms of the iteration number of GLLR solver.

V. CONCLUSION

In this article, a novel structural LR prior is presented for HSI by the structural characteristics. Then we proposed a double LR HSI denoising method by integrating the spatial local smoothing prior. The proposed framework considers both the global LR prior and the local structural LR prior of HSIs. Moreover, via integrating spatial local smoothing, it can retain useful structural information while removing noise in HSIs. The experimental results indicate that the developed GLLR has reliable denoising effectiveness. Nevertheless, there is still limitation of our method, which needs additional considerations for reducing computational costs for possible real-time processing. To address this issue, we have considered several potential strategies to reduce the time cost, such as reducing the number of iterations, the GPU acceleration, and the algorithm simplification. These strategies will be validated in our subsequent work. Furthermore, we believe that the proposed prior has the potential to be extended to joint denoising and subsequent tasks, such as classification and object detection, to ensure that denoising operations optimally serve classification/detection tasks.

REFERENCES

[1] C.-I. Chang and K. Y. Ma, "Band sampling of kernel constrained energy minimization using training samples for hyperspectral mixed pixel classification," *IEEE Trans. Geosci. Remote Sens.*, vol. 60, 2022, Art. no. 5522721.

[2] Z. Gong, L. Tong, J. Zhou, B. Qian, L. Duan, and C. Xiao, "Superpixel spectral–spatial feature fusion graph convolution network for hyperspectral image classification," *IEEE Trans. Geosci. Remote Sens.*, vol. 60, 2022, Art. no. 5536216.

[3] Z. Shu, Z. Liu, J. Zhou, S. Tang, Z. Yu, and X.-J. Wu, "Spatial–spectral split attention residual network for hyperspectral image classification," *IEEE J. Sel. Topics Appl. Earth Observ. Remote Sens.*, vol. 16, pp. 419–430, 2023.

[4] Z. Lv, P. Zhang, W. Sun, J. A. Benediktsson, J. Li, and W. Wang, "Novel adaptive region spectral–spatial features for land cover classification with high spatial resolution remotely sensed imagery," *IEEE Trans. Geosci. Remote Sens.*, vol. 61, 2023, Art. no. 5609412.

[5] S. Zhang, M. Xu, J. Zhou, and S. Jia, "Unsupervised spatial–spectral CNN-based feature learning for hyperspectral image classification," *IEEE Trans. Geosci. Remote Sens.*, vol. 60, 2022, Art. no. 5524617.

[6] J. Peng, Y. Huang, W. Sun, N. Chen, Y. Ning, and Q. Du, "Domain adaptation in remote sensing image classification: A survey," *IEEE J. Sel. Topics Appl. Earth Observ. Remote Sens.*, vol. 15, pp. 9842–9859, 2022.

[7] C.-I. Chang, "Constrained energy minimization anomaly detection for hyperspectral imagery via dummy variable trick," *IEEE Trans. Geosci. Remote Sens.*, vol. 60, 2022, Art. no. 5517119.

[8] C.-I. Chang, H. Cao, S. Chen, X. Shang, C. Yu, and M. Song, "Orthogonal subspace projection-based go-decomposition approach to finding low-rank and sparsity matrices for hyperspectral anomaly detection," *IEEE Trans. Geosci. Remote Sens.*, vol. 59, no. 3, pp. 2403–2429, Mar. 2021.

[9] X. Shang et al., "Target-constrained interference-minimized band selection for hyperspectral target detection," *IEEE Trans. Geosci. Remote Sens.*, vol. 59, no. 7, pp. 6044–6064, Jul. 2021.

[10] Q. Zhang, Y. Zheng, Q. Yuan, M. Song, H. Yu, and Y. Xiao, "Hyperspectral image denoising: From model-driven, data-driven, to model-data-driven," *IEEE Trans. Neural Netw. Learn. Syst.*, early access, Jun. 6, 2023, doi: 10.1109/TNNLS.2023.3278866.

[11] J. Yan, L. Wang, H. He, D. Liang, W. Song, and W. Han, "Large-area land-cover changes monitoring with time-series remote sensing images using transferable deep models," *IEEE Trans. Geosci. Remote Sens.*, vol. 60, 2022, Art. no. 4409917.

[12] Z. Lv, F. Wang, G. Cui, J. A. Benediktsson, T. Lei, and W. Sun, "Spatial–spectral attention network guided with change magnitude image for land cover change detection using remote sensing images," *IEEE Trans. Geosci. Remote Sens.*, vol. 60, 2022, Art. no. 4412712.

[13] D. He, Y. Zhong, and L. Zhang, "Spectral–spatial–temporal MAP-based sub-pixel mapping for land-cover change detection," *IEEE Trans. Geosci. Remote Sens.*, vol. 58, no. 3, pp. 1696–1717, Mar. 2020.

[14] Y. Chen, T.-Z. Huang, W. He, X.-L. Zhao, H. Zhang, and J. Zeng, "Hyperspectral image denoising using factor group sparsity-regularized nonconvex low-rank approximation," *IEEE Trans. Geosci. Remote Sens.*, vol. 60, 2022, Art. no. 5515916.

[15] Q. Zhang, Q. Yuan, M. Song, H. Yu, and L. Zhang, "Cooperated spectral low-rankness prior and deep spatial prior for HSI unsupervised denoising," *IEEE Trans. Image Process.*, vol. 31, pp. 6356–6368, 2022.

[16] J. Xue, Y. Zhao, W. Liao, and J. C. Chan, "Nonlocal low-rank regularized tensor decomposition for hyperspectral image denoising," *IEEE Trans. Geosci. Remote Sens.*, vol. 57, no. 7, pp. 5174–5189, Jul. 2019.

[17] J. Peng et al., "Low-rank and sparse representation for hyperspectral image processing: A review," *IEEE Geosci. Remote Sens. Mag.*, vol. 10, no. 1, pp. 10–43, Mar. 2022.

[18] Y. Chen, W. He, X.-L. Zhao, T.-Z. Huang, J. Zeng, and H. Lin, "Exploring nonlocal group sparsity under transform learning for hyperspectral image denoising," *IEEE Trans. Geosci. Remote Sens.*, vol. 60, 2022, Art. no. 5537518.

[19] H. Zhang, J. Cai, W. He, H. Shen, and L. Zhang, "Double low-rank matrix decomposition for hyperspectral image denoising and destriping," *IEEE Trans. Geosci. Remote Sens.*, vol. 60, 2022, Art. no. 5502619.

[20] W. Sun, J. Peng, G. Yang, and Q. Du, "Fast and latent low-rank subspace clustering for hyperspectral band selection," *IEEE Trans. Geosci. Remote Sens.*, vol. 58, no. 6, pp. 3906–3915, Jun. 2020.

[21] W. Dong et al., "Hyperspectral image super-resolution via non-negative structured sparse representation," *IEEE Trans. Image Process.*, vol. 25, no. 5, pp. 2337–2352, May 2016.

[22] F. Xiong, J. Zhou, and Y. Qian, "Hyperspectral restoration via L_0 gradient regularized low-rank tensor factorization," *IEEE Trans. Geosci. Remote Sens.*, vol. 57, no. 12, pp. 10410–10425, Dec. 2019.

[23] Y. Hou et al., "NLH: A blind pixel-level non-local method for real-world image denoising," *IEEE Trans. Image Process.*, vol. 29, pp. 5121–5135, 2020.

[24] L. Yang, L. Xu, J. Peng, Y. Song, A. Wong, and D. A. Clausi, "Non-local band-weighted iterative spectral mixture model for hyperspectral imagery denoising," *IEEE Trans. Geosci. Remote Sens.*, vol. 58, no. 8, pp. 5588–5601, Aug. 2020.

[25] Q. Yuan, L. Zhang, and H. Shen, "Hyperspectral image denoising employing a spectral–spatial adaptive total variation model," *IEEE Trans. Geosci. Remote Sens.*, vol. 50, no. 10, pp. 3660–3677, Oct. 2012.

[26] M.-H. Cheng, T.-Z. Huang, X.-L. Zhao, T.-H. Ma, and J. Huang, "A variational model with hybrid hyper-Laplacian priors for retinex," *Appl. Math. Model.*, vol. 66, pp. 305–321, Feb. 2019.

[27] J. Li, Q. Yuan, H. Shen, and L. Zhang, "Noise removal from hyperspectral image with joint spectral–spatial distributed sparse representation," *IEEE Trans. Geosci. Remote Sens.*, vol. 54, no. 9, pp. 5425–5439, Sep. 2016.

[28] X.-L. Zhao, J.-H. Yang, T.-H. Ma, T.-X. Jiang, M. K. Ng, and T.-Z. Huang, "Tensor completion via complementary global, local, and nonlocal priors," *IEEE Trans. Image Process.*, vol. 31, pp. 984–999, 2022.

[29] N. Renard, S. Bourennane, and J. Blanc-Talon, "Denoising and dimensionality reduction using multilinear tools for hyperspectral images," *IEEE Geosci. Remote Sens. Lett.*, vol. 5, no. 2, pp. 138–142, Apr. 2008.

[30] L. He, J. Li, A. Plaza, and Y. Li, "Discriminative low-rank Gabor filtering for spectral–spatial hyperspectral image classification," *IEEE Trans. Geosci. Remote Sens.*, vol. 55, no. 3, pp. 1381–1395, Mar. 2017.

[31] H. Zhang, W. He, L. Zhang, H. Shen, and Q. Yuan, "Hyperspectral image restoration using low-rank matrix recovery," *IEEE Trans. Geosci. Remote Sens.*, vol. 52, no. 8, pp. 4729–4743, Aug. 2014.

[32] Y. Peng, J. Suo, Q. Dai, and W. Xu, "Reweighted low-rank matrix recovery and its application in image restoration," *IEEE Trans. Cybern.*, vol. 44, no. 12, pp. 2418–2430, Dec. 2014.

[33] X. Lu, Y. Wang, and Y. Yuan, "Graph-regularized low-rank representation for destriping of hyperspectral images," *IEEE Trans. Geosci. Remote Sens.*, vol. 51, no. 7, pp. 4009–4018, Jul. 2013.

[34] C.-I. Chang and Q. Du, "Interference and noise-adjusted principal components analysis," *IEEE Trans. Geosci. Remote Sens.*, vol. 37, no. 5, pp. 2387–2396, 1999.

[35] W. He, H. Zhang, L. Zhang, and H. Shen, "Total-variation-regularized low-rank matrix factorization for hyperspectral image restoration," *IEEE Trans. Geosci. Remote Sens.*, vol. 54, no. 1, pp. 178–188, Jan. 2016.

[36] Y. Yang, J. Zheng, S. Chen, and M. Zhang, "Hyperspectral image restoration via local low-rank matrix recovery and moreau-enhanced total variation," *IEEE Geosci. Remote Sens. Lett.*, vol. 17, no. 6, pp. 1037–1041, Jun. 2020.

[37] R. Feng, H. Li, L. Wang, Y. Zhong, L. Zhang, and T. Zeng, "Local spatial constraint and total variation for hyperspectral anomaly detection," *IEEE Trans. Geosci. Remote Sens.*, vol. 60, 2022, Art. no. 5512216.

[38] X. Zhang, X. Ma, N. Huyan, J. Gu, X. Tang, and L. Jiao, "Spectral-difference low-rank representation learning for hyperspectral anomaly detection," *IEEE Trans. Geosci. Remote Sens.*, vol. 59, no. 12, pp. 10364–10377, Dec. 2021.

[39] C. Zhao, C. Li, S. Feng, and X. Jia, "Enhanced total variation regularized representation model with endmember background dictionary for hyperspectral anomaly detection," *IEEE Trans. Geosci. Remote Sens.*, vol. 60, 2022, Art. no. 5518312.

[40] Y. Chen, J. Li, and Y. Zhou, "Hyperspectral image denoising by total variation-regularized bilinear factorization," *Signal Process.*, vol. 174, Sep. 2020, Art. no. 107645.

[41] Q. Wang, Z. Wu, J. Jin, T. Wang, and Y. Shen, "Low rank constraint and spatial spectral total variation for hyperspectral image mixed denoising," *Signal Process.*, vol. 142, pp. 11–26, Jan. 2018.

[42] W. He, H. Zhang, H. Shen, and L. Zhang, "Hyperspectral image denoising using local low-rank matrix recovery and global spatial–spectral total variation," *IEEE J. Sel. Topics Appl. Earth Observ. Remote Sens.*, vol. 11, no. 3, pp. 713–729, Mar. 2018.

[43] J. Peng, Y. Wang, H. Zhang, J. Wang, and D. Meng, "Exact decomposition of joint low rankness and local smoothness plus sparse matrices," *IEEE Trans. Pattern Anal. Mach. Intell.*, vol. 45, no. 5, pp. 5766–5781, May 2023.

[44] Z. Lv, H. Huang, L. Gao, J. A. Benediktsson, M. Zhao, and C. Shi, "Simple multiscale UNet for change detection with heterogeneous remote sensing images," *IEEE Geosci. Remote Sens. Lett.*, vol. 19, pp. 1–5, 2022.

[45] A. Maffei, J. M. Haut, M. E. Paoletti, J. Plaza, L. Bruzzone, and A. Plaza, "A single model CNN for hyperspectral image denoising," *IEEE Trans. Geosci. Remote Sens.*, vol. 58, no. 4, pp. 2516–2529, Apr. 2020.

[46] Z. Lv, P. Zhong, W. Wang, Z. You, and N. Falco, "Multiscale attention network guided with change gradient image for land cover change detection using remote sensing images," *IEEE Geosci. Remote Sens. Lett.*, vol. 20, pp. 1–5, 2023.

[47] Q. Zhang, Q. Yuan, Z. Li, F. Sun, and L. Zhang, "Combined deep prior with low-rank tensor SVD for thick cloud removal in multitemporal images," *ISPRS J. Photogramm. Remote Sens.*, vol. 177, pp. 161–173, Jul. 2021.

[48] Q. Zhang, Q. Yuan, J. Li, F. Sun, and L. Zhang, "Deep spatio-spectral Bayesian posterior for hyperspectral image non-i.I.d. noise removal," *ISPRS J. Photogramm. Remote Sens.*, vol. 164, pp. 125–137, Jun. 2020.

[49] X. Cao, X. Fu, C. Xu, and D. Meng, "Deep spatial–spectral global reasoning network for hyperspectral image denoising," *IEEE Trans. Geosci. Remote Sens.*, vol. 60, 2022, Art. no. 5504714.

[50] F. Xiong, J. Zhou, S. Tao, J. Lu, J. Zhou, and Y. Qian, "SMDS-Net: Model guided spectral–spatial network for hyperspectral image denoising," *IEEE Trans. Image Process.*, vol. 31, pp. 5469–5483, 2022.

[51] Q. Zhang, Q. Yuan, J. Li, X. Liu, H. Shen, and L. Zhang, "Hybrid noise removal in hyperspectral imagery with a spatial–spectral gradient network," *IEEE Trans. Geosci. Remote Sens.*, vol. 57, no. 10, pp. 7317–7329, Oct. 2019.

[52] Q. Yuan, Q. Zhang, J. Li, H. Shen, and L. Zhang, "Hyperspectral image denoising employing a spatial–spectral deep residual convolutional neural network," *IEEE Trans. Geosci. Remote Sens.*, vol. 57, no. 2, pp. 1205–1218, Feb. 2019.

[53] Q. Zhang, Q. Yuan, J. Li, Z. Li, H. Shen, and L. Zhang, "Thick cloud and cloud shadow removal in multitemporal imagery using progressively spatio-temporal patch group deep learning," *ISPRS J. Photogramm. Remote Sens.*, vol. 162, pp. 148–160, Apr. 2020.

[54] R. Dian, T. Shan, W. He, and H. Liu, "Spectral super-resolution via model-guided cross-fusion network," *IEEE Trans. Neural Netw. Learn. Syst.*, early access, Jan. 27, 2023, doi: 10.1109/TNNLS.2023.3238506.

[55] R. Dian, S. Li, and L. Fang, "Learning a low tensor-train rank representation for hyperspectral image super-resolution," *IEEE Trans. Neural Netw. Learn. Syst.*, vol. 30, no. 9, pp. 2672–2683, Sep. 2019.

[56] D. He and Y. Zhong, "Deep hierarchical pyramid network with high-frequency-aware differential architecture for super-resolution mapping," *IEEE Trans. Geosci. Remote Sens.*, vol. 61, 2023, Art. no. 5503815.

[57] Z. Zhou, X. Li, J. Wright, E. Candès, and Y. Ma, "Stable principal component pursuit," in *Proc. IEEE Int. Symp. Inf. Theory*, Jun. 2010, pp. 1518–1522.

[58] L. Chen, F. Fang, T. Wang, and G. Zhang, "Blind image deblurring with local maximum gradient prior," in *Proc. IEEE/CVF Conf. Comput. Vis. Pattern Recognit. (CVPR)*, Jun. 2019, pp. 1742–1750.

[59] A. H. Abdelmeguid, A. Youssif, and G. M. I. Selim, "Blind facial images deblurring using dark channel prior," in *Proc. Int. Conf. Appl. Math. Comput. Sci. (ICAMCS)*, Apr. 2018, pp. 35–356.

[60] D. L. Donoho, "De-noising by soft-thresholding," *IEEE Trans. Inf. Theory*, vol. 41, no. 3, pp. 613–627, May 1995.

[61] D. Krishnan and R. Fergus, "Fast image deconvolution using hyper-Laplacian priors," in *Proc. Adv. Neural Inf. Process. Syst.*, vol. 22, 2009, pp. 1033–1041.

[62] E. J. Candès, X. Li, Y. Ma, and J. Wright, "Robust principal component analysis?" *J. ACM*, vol. 58, no. 1, pp. 1–37, 2009.

[63] Y. Peng, D. Meng, Z. Xu, C. Gao, Y. Yang, and B. Zhang, "Decomposable nonlocal tensor dictionary learning for multispectral image denoising," in *Proc. IEEE Conf. Comput. Vis. Pattern Recognit.*, Jun. 2014, pp. 2949–2956.

[64] W. He et al., "Non-local meets global: An iterative paradigm for hyperspectral image restoration," *IEEE Trans. Pattern Anal. Mach. Intell.*, vol. 44, no. 4, pp. 2089–2107, Apr. 2022.

[65] J. M. Bioucas-Dias and J. M. P. Nascimento, "Hyperspectral subspace identification," *IEEE Trans. Geosci. Remote Sens.*, vol. 46, no. 8, pp. 2435–2445, Aug. 2008.

Lan Li received the B.S. degree in software engineering from Chaohu University, Chaohu, China, in 2018, and the M.S. degree in computer technology from Dalian Maritime University, Dalian, China, in 2021, where she is currently pursuing the Ph.D. degree with the School of Information Science and Technology.

Her research interests include remote sensing information processing.

Meiping Song (Member, IEEE) received the Ph.D. degree from the College of Computer Science and Technology, Harbin Engineering University, Harbin, China, in 2006.

She has been a Professor with the College of Information Science and Technology, Dalian Maritime University, Dalian, China, since 2020. Her research interests include remote sensing and hyperspectral image processing.

Qiang Zhang (Member, IEEE) received the B.E. degree in surveying and mapping engineering and the M.E. and Ph.D. degrees in photogrammetry and remote sensing from Wuhan University, Wuhan, China, in 2017, 2019, and 2022, respectively.

He is currently an Associate Professor with the Center of Hyperspectral Imaging in Remote Sensing (CHIRS), Information Science and Technology College, Dalian Maritime University, Dalian, China. He has authored more than ten journal articles in the IEEE TRANSACTIONS ON IMAGE PROCESSING (TIP), IEEE TRANSACTIONS ON GEOSCIENCE AND REMOTE SENSING (TGRS), *Earth System Science Data* (ESSD), and *ISPRS Journal of Photogrammetry and Remote Sensing* (P&RS). His research interests include remote sensing information processing, computer vision, and machine learning. More details could be found at https://qzhang95.github.io.

Yushuai Dong received the B.S. degree in food science and engineering from Huazhong Agricultural University, Wuhan, China, in 2022. He is currently pursuing the M.S. degree with the Information Science and Technology College, Dalian Maritime University, Dalian, China.

His research interests include hyperspectral image processing and machine learning.